TASK QUARTERLY 13 No 1–2, 45–73

GODUNOV-TYPE NUMERICAL METHODS FOR ONE- AND TWO-COMPONENT MAGNETOHYDRODYNAMIC EQUATIONS

KRZYSZTOF MURAWSKI

Institute of Physics, UMCS,
Radziszewskiego 10, 20-031 Lublin, Poland
kmur@kft.umcs.lublin.pl

(Received 13 August 2008)

Abstract: In this paper we review Godunov-type numerical methods for one- and two-component magnetohydrodynamic equations. Solving these equations numerically is a formidable task as a result of the internal complexity of these equations and the requirements of $\nabla \cdot \mathbf{B} = 0$. We present several results of advanced numerical simulations for complex systems. These results prove that the numerical codes which are based on Godunov-type methods, cope with all problems very well.

Keywords: numerical simulations of hyperbolic equations, Godunov methods, magnetohydrodynamics

1. Introduction

Plasma generally exhibits both collective (fluid-like) and individual (particle-like) behavior. In the magnetohydrodynamic model, plasma is treated like a conducting fluid having macroscopic parameters that accurately describe its particle-like interactions, *e.g.* [1]. This model combines fluid equations and Maxwell's equations. Although the MHD theory is the simplest self-consistent model describing the macroscopic behavior of plasma, the full nonlinear equations are so complex that simplifications are usually necessary to yield tractable problems. Therefore, many solutions require numerical treatment. Finite-volume methods are one of several different techniques available to solve the MHD equations. They are simple to implement, easily adaptable to complex geometries, and well suited to handle nonlinear terms.

Similarly to solutions of hydrodynamic and other hyperbolic equations solutions of MHD equations exhibit the tendency to form large gradients (*e.g.* shock waves) which are difficult for numerical modeling. The use of standard numerical schemes of second-order accuracy or higher (*e.g.* the Lax-Fredrichs method) generates spurious oscillations which destroy the solution's monotonicity. Lower-order schemes, *e.g.* [2] are generally free of oscillations, but they are dissipative enough to wash out much of

the details. Therefore, there is a need to develop more advanced schemes which would adequately represent the large gradient profiles.

The aim of this paper is to review the numerical methods for solving one- and two-component MHD equations. In particular, in Section 2 we discuss most of the problems which are associated with numerical solutions of these equations. Sections 3 and 4 present conservative and non-conservative forms of MHD equations. The eigenvalue problem of the Jacobian that results from quasi-linearization of these equations is discussed in Section 5. Singularities which result in the eigen-value problem are presented in Section 6. A Riemann problem is explored in Section 7. Numerical schemes that clean the selenoidal condition are illustrated in Section 8. A Riemann problem for two-component MHD equations is discussed in Section 9. The results of numerical simulations for waves in a coronal loop and for solar wind interaction with a non-magnetic body are presented in Sections 10 and 11, respectively. The paper is completed by the following section which summarizes the main results of this paper.

2. Problems with MHD equations

It is not a straightforward task to convert an Euler code to a MHD code since various kinds of singularities are present in the MHD equations. Moreover, due to the intrinsic complexity of the MHD equations, the development of numerical techniques to solve these equations has been slower than for hydrodynamics (HD). For instance, for a long time, most numerical schemes have been based on methods dependent on artificial viscosity to represent shocks adequately, *e.g.* [3]. Although these schemes have been used successfully in astrophysical applications, *e.g.* [4, 5], the past experience with fully conservative, high-order upwind hydrodynamic codes found those to be superior in many applications [6]. It is therefore natural to extend such schemes to solve MHD conservation equations. However, there are two principal difficulties associated with the numerical solution of MHD equations as compared to hydrodynamic (HD) equations [7]. The first difficulty is that MHD equations possess new families of waves. Moreover, MHD admits a variety of exotic wave structures such as switch-on fast shocks, switch-off fast rarefactions, switch-off slow shocks, and switch-on slow rarefactions. It is also possible to obtain compound waves of either fast or slow waves. This has a considerable impact on the performance of algorithms which are required to provide a stable and accurate capture of this entire range of such structures, *e.g.* [8]. Roe and Balsara [7] list six cases that can potentially cause trouble.

Another difficulty is that the MHD equations contain a magnetic field which has to satisfy the divergence-free constraint, $\nabla \cdot \mathbf{B} = 0$. A local nonzero divergence of the magnetic field indicates the existence of magnetic monopoles within the numerical cell which leads to nonconservation of the magnetic flux across its surface. Accumulation of the numerical errors associated with evolving the magnetic field components can lead to a violation of this constraint, causing an artificial force parallel to the magnetic field, and eventually it can force termination of the simulations.

Despite these problems, many numerical schemes have been developed for the MHD equations. These schemes reveal either conservative or non-conservative properties of the equations.

3. Conservative form of the MHD equations

The MHD equations can be written in the conservative form:

$$\mathbf{u}_{,t}+\nabla\cdot\mathbf{f}=0,\quad \nabla\cdot\mathbf{B}=0, \tag{1}$$

where:

$$\mathbf{u}=(\varrho,\varrho\mathbf{v},\mathbf{B},E)^T, \tag{2}$$

$$\mathbf{f}=(\varrho\mathbf{v},\varrho\mathbf{v}\mathbf{v}+\mathbf{I}(p+\frac{B^2}{2})-\mathbf{B}\mathbf{B},\mathbf{v}\mathbf{B}-\mathbf{B}\mathbf{v}, \tag{3}$$

$$(E+p+\frac{B^2}{2})\mathbf{v}-\mathbf{B}(\mathbf{v}\cdot\mathbf{B}))^T. \tag{4}$$

Here $\mathbf{I}$ is the 3×3 identity matrix, $\mathbf{vv}$ stands for the 3×3 tensor v_iv_j, and $\mathbf{B}$ has been normalized by $\sqrt{\mu}$.

The momentum equation of (1) can be rewritten as follows:

$$(\varrho\mathbf{v})_{,t}+\nabla\cdot(\varrho\mathbf{v}\mathbf{v})+\nabla(p+\frac{B^2}{2})-(\mathbf{B}\cdot\nabla)\mathbf{B}-\mathbf{B}(\nabla\cdot\mathbf{B})=0. \tag{5}$$

The last term of this equation should be equal to zero. If nevertheless $\nabla\cdot\mathbf{B}$ differs from zero, it becomes an additional unphysical force which is parallel to $\mathbf{B}$. This force has a destabilizing effect on numerical algorithms. Brackbill and Barnes [9] have noted that this instability can be removed by adding the term $-\mathbf{B}(\nabla\cdot\mathbf{B})$ to the right hand side of Equation (5). This procedure leads to a non-conservative form of the MHD equations.

The plasma state of Equation (2)in the finite volume method is advanced in time by evaluating the fluxes of Equation (4) at the interfaces between neighboring states. In order for the Rankine-Hugoniot conditions to be satisfied at these interfaces, these fluxes must contain some kind of dissipation and a flux limiter must be applied to minimize the post-shock oscillation. To eliminate these oscillations, a spatially averaged primitive state,

$$\tilde{\mathbf{u}}=(\bar{\varrho},\bar{\mathbf{v}},\bar{\mathbf{B}},\bar{E})^T \tag{6}$$

is required at the interfaces. Brio and Wu [10] have concluded that such averaging is possible only for the case of $\gamma=2$.

4. Non-conservative equations

The MHD equations can be written in a non-conservative form [11]:

$$\mathbf{u}_{,t}+\nabla\cdot\mathbf{f}=-\nabla\cdot\mathbf{B}(0,\mathbf{B},\mathbf{v},\mathbf{v}\cdot\mathbf{B})^T,\quad \nabla\cdot\mathbf{B}=0. \tag{7}$$

It is interesting to check how this change effects the induction equation which can be now written as:

$$\mathbf{B}_{,t}+\mathbf{v}(\nabla\cdot\mathbf{B})+\mathbf{B}(\nabla\cdot\mathbf{v})-(\mathbf{B}\cdot\nabla)\mathbf{v}=0. \tag{8}$$

Taking the divergence of both sides and using the mass continuity equation, we obtain an advection equation for the quantity $\nabla\cdot\mathbf{B}/\varrho$, *i.e.*:

$$\left(\frac{\nabla\cdot\mathbf{B}}{\varrho}\right)_{,t}+\mathbf{v}\cdot\nabla\left(\frac{\nabla\cdot\mathbf{B}}{\varrho}\right)=0. \tag{9}$$

As a consequence of that we have introduced a new *divergence wave* which propagates with the speed $\mathbf{v}$. Thus, a partially conservative form of the multi-dimensional equations, obtained by adding terms proportional to $\nabla\cdot\mathbf{B}$, retains the one-dimensional eigen-value problem, with the addition of an eighth wave that convects $\nabla\cdot\mathbf{B}$ as a passive scalar.

The original MHD equations can be written in a quasilinear form:

$$\bar{\mathbf{u}}_{,t}+\mathbf{A}\bar{\mathbf{u}}_{,x}=0, \tag{10}$$

where:

$$\bar{\mathbf{u}}=(\varrho,\varrho\mathbf{v},\mathbf{B},p)^T, \tag{11}$$

$$\mathbf{A}=\begin{pmatrix} v_x & \varrho & 0 & 0 & 0 & 0 & 0 & 0\\ 0 & v_x & 0 & 0 & -\frac{B_x}{\varrho} & \frac{B_y}{\varrho} & \frac{B_z}{\varrho} & \frac{1}{\varrho}\\ 0 & 0 & v_x & 0 & -\frac{B_y}{\varrho} & -\frac{B_x}{\varrho} & 0 & 0\\ 0 & 0 & 0 & v_x & -\frac{B_z}{\varrho} & 0 & -\frac{B_x}{\varrho} & 0\\ 0 & 0 & 0 & 0 & 0 & 0 & 0 & 0\\ 0 & B_y & -B_x & 0 & -v_y & v_x & 0 & 0\\ 0 & B_z & 0 & -B_x & -v_z & 0 & v_x & 0\\ 0 & \gamma p & 0 & 0 & (\gamma-1)\mathbf{v}\cdot\mathbf{B} & 0 & 0 & v_x \end{pmatrix}. \tag{12}$$

It is noteworthy that the 5-th row from the top of the matrix $\mathbf{A}$ consists of zeros. This is a consequence of the fact that $(\nabla\cdot\mathbf{B})_{,t}=0$. As a result of the zero row, we find that the 8-th eigenvalue of $\mathbf{A}$ is zero, *i.e.*:

$$w^8{}_{,t}+0w^8{}_{,x}=0, \tag{13}$$

where $w^8=B_x$.

Equation (7) for $\mathbf{u}=\bar{\mathbf{u}}$ can be written as:

$$\bar{\mathbf{u}}_{,t}+\mathbf{A}\bar{\mathbf{u}}_{,x}=-\begin{pmatrix} 0 & 0 & 0 & 0 & 0 & 0 & 0 & 0\\ 0 & 0 & 0 & 0 & \frac{B_x}{\varrho} & 0 & 0 & 0\\ 0 & 0 & 0 & 0 & \frac{B_y}{\varrho} & 0 & 0 & 0\\ 0 & 0 & 0 & 0 & \frac{B_z}{\varrho} & 0 & 0 & 0\\ 0 & 0 & 0 & 0 & v_x & 0 & 0 & 0\\ 0 & 0 & 0 & 0 & v_y & 0 & 0 & 0\\ 0 & 0 & 0 & 0 & v_z & 0 & 0 & 0\\ 0 & 0 & 0 & 0 & (\gamma-1)\mathbf{v}\cdot\mathbf{B} & 0 & 0 & 0 \end{pmatrix}\bar{\mathbf{u}}_{,x}, \tag{14}$$

where $\mathbf{A}$ is the matrix defined by Equation (11). This equation can be rewritten in a quasilinear form:

$$\bar{\mathbf{u}}_{,t}+\bar{\mathbf{A}}\bar{\mathbf{u}}_{,x}=0, \tag{15}$$

where:

$$\bar{\mathbf{A}}=\begin{pmatrix} v_x & \varrho & 0 & 0 & 0 & 0 & 0 & 0\\ 0 & v_x & 0 & 0 & 0 & \frac{B_y}{\varrho} & \frac{B_z}{\varrho} & \frac{1}{\varrho}\\ 0 & 0 & v_x & 0 & 0 & -\frac{B_x}{\varrho} & 0 & 0\\ 0 & 0 & 0 & v_x & 0 & 0 & -\frac{B_x}{\varrho} & 0\\ 0 & 0 & 0 & 0 & v_x & 0 & 0 & 0\\ 0 & B_y & -B_x & 0 & 0 & v_x & 0 & 0\\ 0 & B_z & 0 & -B_x & 0 & 0 & v_x & 0\\ 0 & \gamma p & 0 & 0 & 0 & 0 & 0 & v_x \end{pmatrix}. \tag{16}$$

Thus, we can see that the zero row has disappeared and the eight wave now satisfies the advection equation:

$$w^8{}_{,t} + v_x w^8{}_{,x} = 0. \tag{17}$$

As this wave carries non-zero magnetic field divergence it is nicknamed the *divergence* wave.

5. Eigenvalues and eigenvectors

The Jacobian matrix $\bar{\mathbf{A}}$ has the eigenvalues (λ) and left ($\mathbf{l}$) and right ($\mathbf{r}$) eigenvectors which correspond to the following waves [11]:

- Four magnetosonic waves with:

$$\lambda^{\pm} = v_x \pm c_{\pm}, \tag{18}$$

$$\mathbf{l}^{\pm} = N^{\pm} \begin{pmatrix} 0 \\ \pm\varrho c_{\pm} \\ \mp\frac{B_x B_y \varrho c_{\pm}}{\varrho c_{\pm}^2 - B_x^2} \\ \mp\frac{B_x B_z \varrho c_{\pm}}{\varrho c_{\pm}^2 - B_x^2} \\ 0 \\ \frac{B_y \varrho c_{\pm}^2}{\varrho c_{\pm}^2 - B_x^2} \\ \frac{B_z \varrho c_{\pm}^2}{\varrho c_{\pm}^2 - B_x^2} \\ 1 \end{pmatrix}^T, \qquad \mathbf{r}^{\pm} = N^{\pm} \begin{pmatrix} \varrho \\ \pm c_{\pm} \\ \mp\frac{B_x B_y c_{\pm}}{\varrho c_{\pm}^2 - B_x^2} \\ \mp\frac{B_x B_z c_{\pm}}{\varrho c_{\pm}^2 - B_x^2} \\ 0 \\ \frac{B_y \varrho c_{\pm}^2}{\varrho c_{\pm}^2 - B_x^2} \\ \frac{B_z \varrho c_{\pm}^2}{\varrho c_{\pm}^2 - B_x^2} \\ \gamma p \end{pmatrix}, \tag{19}$$

  where $N^{\pm}$ stands for a normalization factor such that $\mathbf{l}^{\pm}\mathbf{r}^{\pm} = 1$. This factor is too complicated to be printed here. The superscript $\pm$ corresponds to the fast (c_+) and slow (c_-) magnetosonic wave speeds;
- Two Alfvén waves with:

$$\lambda^a = v_x \pm V_A, \tag{20}$$

$$\mathbf{l}^a = \frac{1}{2\sqrt{N}}(0,0,-B_z,B_y,0,\pm\frac{B_z}{\sqrt{\varrho}},\mp\frac{B_y}{\sqrt{\varrho}},0), \tag{21}$$

$$\mathbf{r}^a = \frac{1}{\sqrt{N}}(0,0,-B_z,B_y,0,\pm B_z\sqrt{\varrho},\mp B_y\sqrt{\varrho},0)^T, \tag{22}$$

  where $N = 1/(B_y^2 + B_z^2)$ is a normalized factor and the Alfvén speed $V_A = B_x/\sqrt{\varrho}$;
- One entropy wave with:

$$\lambda^e = v_x, \tag{23}$$

$$\mathbf{l}^e = (1,0,0,0,0,0,0,\frac{-1}{c_s^2}), \tag{24}$$

$$\mathbf{r}^e = (1,0,0,0,0,0,0,0)^T. \tag{25}$$

  Here the entropy s is defined as:

$$s = log\left(\frac{p}{\varrho^{\gamma}}\right); \tag{26}$$

- One divergence wave with:

$$\lambda^{div} = v_x, \tag{27}$$

$$\mathbf{l}^{div}=(0,0,0,0,1,0,0,0), \tag{28}$$

$$\mathbf{r}^{div}=(0,0,0,0,1,0,0,0)^T. \tag{29}$$

6. Singularities

The Alfvén eigenvectors become singular when:

$$B_\perp\equiv\sqrt{B_y^2+B_z^2}\to 0. \tag{30}$$

The magnetosonic eigenvectors are singular for $c_\pm^2\to V_A^2$, $c_+^2\to c_-^2$. In the latter limit, the wavespeeds c_-, c_+, and V_A coincide. These singularities have to be considered before writing any code. The first solution to this problem was provided by Brio [12]. Another approach was made by Zachary and Colella [13]. We describe it in some details in the text below.

Let us define:

$$\beta_y=\frac{B_y}{B_\perp},\quad \beta_z=\frac{B_z}{B_\perp}. \tag{31}$$

Then, the Alfvén eigenvectors can be written as follows:

$$\mathbf{l}^{a\pm}=\frac{1}{2}\left(0,0,\pm\beta_z,\mp\beta_y,0,-\frac{\beta_z sgn(B_x)}{\sqrt{\varrho}},\frac{\beta_y sgn(B_x)}{\sqrt{\varrho}},0\right), \tag{32}$$

$$\mathbf{r}^{a\pm}=(0,0,\pm\beta_z,\mp\beta_y,0,-\beta_z\sqrt{\varrho}sgn(B_x),\beta_y\sqrt{\varrho}sgn(B_x),0)^T. \tag{33}$$

The singularities in the Alfvén speed can be fixed by applying [10]:

$$\lim_{B_\perp\to 0}\beta_y=\lim_{B_\perp\to 0}\beta_z=\frac{1}{\sqrt{2}}. \tag{34}$$

An elegant way of implementing the above limit into a code is to set:

$$\beta_y=\frac{B_y+\epsilon}{B_\perp+\epsilon\sqrt{2}},\quad \epsilon<<1. \tag{35}$$

Now, we define:

$$\alpha_-^2=\frac{c_s^2-c_-^2}{c_+^2-c_-^2},\quad \alpha_+^2=\frac{c_+^2-c_s^2}{c_+^2-c_-^2}. \tag{36}$$

A lengthy algebra leads to the eigenvectors for the magnetosonic waves [14]:

$$\mathbf{l}^+=\frac{1}{2c_s^2}\begin{pmatrix}0\\ \pm\alpha_+c_+\\ \mp\alpha_-c_-\beta_y sgn(B_x)\\ \mp\alpha_-c_-\beta_z sgn(B_x)\\ 0\\ \alpha_-c_s\beta_y/\sqrt{\varrho}\\ \alpha_-c_s\beta_z/\sqrt{\varrho}\\ \alpha_+/\varrho\end{pmatrix}^T,\qquad \mathbf{r}^+=\begin{pmatrix}\alpha_+\varrho\\ \pm\alpha_+c_+\\ \mp\alpha_-c_-\beta_y sgn(B_x)\\ \mp\alpha_-c_-\beta_z sgn(B_x)\\ 0\\ \alpha_-c_s\beta_y\sqrt{\varrho}\\ \alpha_-c_s\beta_z\sqrt{\varrho}\\ \alpha_+\varrho c_s^2\end{pmatrix}, \tag{37}$$

$$\mathbf{l}^-=\frac{1}{2c_s^2}\begin{pmatrix}0\\ \pm\alpha_-c_-\\ \pm\alpha_+c_+\beta_y sgn(B_x)\\ \pm\alpha_+c_+\beta_z sgn(B_x)\\ 0\\ -\alpha_+c_s\beta_y/\sqrt{\varrho}\\ -\alpha_+c_s\beta_z/\sqrt{\varrho}\\ \alpha_-/\varrho\end{pmatrix}^T,\qquad \mathbf{r}^-=\begin{pmatrix}\alpha_-\varrho\\ \pm\alpha_-c_-\\ \pm\alpha_+c_+\beta_y sgn(B_x)\\ \pm\alpha_+c_+\beta_z sgn(B_x)\\ 0\\ -\alpha_+c_s\beta_y\sqrt{\varrho}\\ -\alpha_+c_s\beta_z\sqrt{\varrho}\\ \alpha_-\varrho c_s^2\end{pmatrix}. \tag{38}$$

These eigenvectors contain only the singularity which is called a triple umbilic T. It occurs at $c_+^2 = c_-^2 = V_A^2$ when $B_\perp \to 0$. The triple umbilic point is, where the fast, slow, and Alfvén speeds coincide. It can be shown that around this point:

$$\alpha_- = \cos\frac{\alpha}{2} + \delta_-, \quad \alpha_+ = \sin\frac{\alpha}{2} + \delta_+, \tag{39}$$

where:

$$\tan\alpha \equiv \frac{B_x - c_s\sqrt{\varrho}}{B_\perp}. \tag{40}$$

The errors $\delta_\pm$ satisfy:

$$|\delta_\pm| \leq \frac{B_\perp}{4c_s\sqrt{\varrho}}. \tag{41}$$

For $B_\perp = 0$ it can be proved that $\alpha_- = H(B_x - c_s\sqrt{\varrho})$ and $\alpha_+ = H(c_s\sqrt{\varrho} - B_x)$, where H is the Heaviside function.

7. Problems with MHD Riemann solver

An important problem in developing a scheme for MHD equations is that these equations are neither strictly hyperbolic nor strictly convex, *e.g.* [10]. The MHD equations form a non-strictly hyperbolic system as some eigenvalues may coincide at some points and compound wave structures, involving both shocks and rarefactions may sometimes develop. It occurs that when the magnetic field components are equal to zero the eigenvectors become singular. These singularities can be removed by renormalizing the eigenvectors [7, 12]. See also the comment at the end of Section 6.

Contrary to the hydrodynamic case, the Riemann problem for ideal MHD is not completely consistent and unique as one of the Jacobian matrix eigenvalues is zero. See Equation (13). This zero eigenvalue is non-physical as the eigenvalues should appear either singly as the x-component of the flow, v_x, or in pairs symmetric about v_x. Physical eigenvalues are given by Equations (18)–(29).

The zero eigenvalue leads to numerical difficulties associated with nonzero divergence of the magnetic field. Consequently, the characteristics can become degenerate, depending on the orientation of the magnetic field. It turns out that the solution of this problem is to consider a form of the equations that is not strictly in a conservation form [11]. See Equation (7).

8. Divergence cleaning schemes

There are several important issues in developing a new MHD code. One of these is ensuring $\nabla\cdot\mathbf{B} = 0$, *e.g.* [15]. It is well known that incorrect treatment of an induction equation will lead to a non-selenoidal field that varies in time, and hence, causes the magnetic field to exert a non-physical force along field lines. It occurs that discretization errors lead to a non-zero divergence over time. Physically, this means that nothing maintains conservation of a magnetic flux in the Gauss' law. This error usually grows exponentially during the computations, causing an artificial force parallel to the magnetic field, unphysical plasma transport orthogonal to $\mathbf{B}$ as well as a loss of momentum and energy conservation, destroying the correctness of the solutions [9]. Several remedies have been proposed. Brackbill and Barnes [9] have found that the momentum equation can be reformulated into a non-conservative

form to eliminate the parallel force. Harder (1987) has proposed a method of adding a diffusion term in the induction equation that makes the divergence-free error diffuse away from the source. Magnetic monopoles are locally suppressed by this term but they are not completely eliminated. Ewans and Hawley (1988) have utilized a numerical technique called *constraint transport* to transform the induction equation in such a way that it maintains a vanishing divergence of the field components to within machine round-off error by placing field components at appropriate locations of a numerical cell. This technique was used by Stone and Norman [3] who implemented a covariant formalism in the ZEUS code based on the finite-differences method. In another constraint transport method, a magnetic field is kept divergence-free to within machine round-off error by placing the magnetic field components at the interface locations of the finite-difference grid [16].

Until recently, there were four traditional approaches to enforce the divergence-free constraint:

(a) a magnetic vector potential, $\mathbf{B}=\nabla\times\mathbf{A}$, approach. Then, the divergence-free condition is satisfied automatically. The difficulty with this approach is that the Lorentz force representation requires taking a second derivative of the vector potential $\mathbf{A}$. This forces an application of higher-order numerical schemes. Even then, serious problems can be encountered due to the anomalous Lorentz force which apparently reveals itself in the neighborhood of large gradients;

(b) a projection scheme which forces the divergence-free constraint by solving a Poisson equation to subtract off the portion of the magnetic field that leads to non-zero divergence, *e.g.* [17]. The essence of this method is as follows. Let us suppose that a magnetic field has a non-zero divergence, $\nabla\cdot\mathbf{B}\neq 0$. We can fix this problem by adding a correction term $\mathbf{B}_c$ such that:

$$\nabla\cdot(\mathbf{B}+\mathbf{B}_c)=0. \tag{42}$$

Clearly, $\mathbf{B}_c$ must not generate new current $\mathbf{j}_c=\frac{1}{\mu}(\nabla\times\mathbf{B}_c)=0$. Hence,

$$\nabla\times\mathbf{B}_c=0, \tag{43}$$

from which we conclude that:

$$\mathbf{B}_c=\nabla\phi, \tag{44}$$

where ϕ is a scalar potential. Substituting Equation (44) into Equation (42) we obtain:

$$\nabla^2\phi=-\nabla\cdot\mathbf{B}. \tag{45}$$

This is the Poisson equation which has to be solved in the whole computational domain. The resulting solution ϕ should be used to evaluate $\mathbf{B}_c$ according to Equation (44) and this to clean the magnetic field $\mathbf{B}$.

This method has its disadvantages. Its major drawback is that it requires a global solution to the elliptic Equation (45) which is computationally expensive. Moreover, the global nature of the cleaning procedure violates the hyperbolicity of the MHD equations in regions where the flow is supersonic and superalfvénic;

(c) a staggered-grid approach in which the divergence-free constraint is satisfied by placing the magnetic field components at the centroids of appropriate cell faces

and volumetric variables such as mass, momentum and energy are stored at the centroids of computational cells. The MHD equations on such a grid can be approximated in a way that preserves the selenoidality of a discrete magnetic field [3, 16]. This approach comes from incompressible fluid mechanics where the velocity field must be kept divergence-free.

Staggered grids are expensive for storage and handling on meshes with hanging nodes that are common to unstructured grid methods. Moreover, appropriate Riemann solvers do not seem to work on staggered grids;

(d) the truncation-level error method which has been developed by Powell [11]. See also [18–20]. That approach relies on an addition to the original set of MHD equations the source term that is proportional to $\nabla\cdot\mathbf{B}$. See Equation (7). By that way any local $\nabla\cdot\mathbf{B}$ that is created is convected away in accordance with Equation (9). That approach leads to the Riemann problem which has an eight-wave structure, where seven of the waves are those used in previous works on upwind methods, *e.g.* [21] for MHD, and the eight wave is associated with the the magnetic field divergence. It has been found by Janhunen [22] that in the case when the contribution to the total energy from the fluid pressure is small in comparison to the magnetic and kinetic energies this approach may lead to an unphysical intermediate state with negative fluid pressure. As a consequence of such computing, the pressure from the conserved quantities may involve the difference between two nearly equal terms and the errors result. Janhunen [22] has shown that this problem can be overcome by discarding the source terms in the energy and momentum equations, so that Equation (7) becomes:

$$\mathbf{u}_{,t}+\nabla\cdot\mathbf{f}=-\nabla\cdot\mathbf{B}(0,0,\mathbf{v},0)^T,\quad \nabla\cdot\mathbf{B}=0. \tag{46}$$

This equation has been derived from relativistic energy-momentum conservation by Dellar [15].

The question of divergence cleaning in a rather detailed way is taken up by Balsara [23, 24]. Essentially, it boils down to saying that if the equations were exactly solved in a discrete fluid dynamic code the divergence would stay at zero as if it had been zero initially. In reality some small errors are made with every time-step. It is only after a lot of time-steps that the errors build up. (This happens in the 7-th or 8-th wave models.) Thus, the cure of removing the divergence needs to be applied only once in a while. Numerical experiments comparing various schemes with respect to the $\nabla\cdot\mathbf{B}=0$ constraint have been recently performed by Tóth [25] who has shown that the truncation-level error method performs generally well. However, this method accumulates so much magnetic monopoles in strongly discontinuous and stagnated flows that they corrupt the solution.

9. A 9-th wave Riemann solver for two-component MHD equations

To discuss the 9-th wave Riemann solver for two-component MHD equations it is useful to denote densities of two-component plasma by ϱ_1 and ϱ_2. Then, the total density is:

$$\varrho=\varrho_1+\varrho_2. \tag{47}$$

The background potential field and source term are expressed by $\mathbf{B}_0$ and $\mathbf{S}$, respectively. Introducing new dependent variables:

$$\begin{aligned}\mathbf{u}_1 &= (\varrho, \mathbf{m}, \mathbf{B}_1, E_1, \varrho_2)^T = (\varrho, m_x, m_y, m_z,\\ B_x - B_{0x}, B_y - B_{0y}, B_z - B_{0z}, E - (\mathbf{B}_1 \cdot \mathbf{B}_0)/\mu - B_0^2/(2\mu), \varrho_2)^T,\end{aligned} \tag{48}$$

with the rotation of dependent variables:

$$\begin{aligned}\mathbf{u}_n &= \mathbf{T}\mathbf{u} = (\varrho, \mathbf{m}_n, \mathbf{B}_n, E, \varrho_2)^T =\\ &(\varrho, m_n, m_{t1}, m_{t2}, B_n, B_{t1}, B_{t2}, E, \varrho_2)^T,\end{aligned} \tag{49}$$

the equation for $\mathbf{u}_1$ can be written as [26]:

$$\frac{\partial}{\partial t}\int \mathbf{u}_1 dv + \int \mathbf{T}^{-1}\mathbf{F}(\mathbf{u}_{1n}, \mathbf{B}_{0n}) ds = \int \mathbf{S} dv, \tag{50}$$

where dv and ds are the volume and surface elements of the control volume and $\mathbf{T}$ is a matrix which rotates the x-axis to the direction of a unit vector $\mathbf{n}$ normal to the control volume surface. The flux function $\mathbf{F}$ in the normalized form is written as:

$$\mathbf{F} = \begin{pmatrix} m_n \\ p + \frac{m_n m_n}{\varrho} + \frac{B^2}{2\mu} - \frac{1}{\mu} B_n B_n - \frac{B_0^2}{2\mu} + \frac{1}{\mu} B_{0n} B_{0n} \\ \frac{m_{t1} m_n}{\varrho} - \frac{1}{\mu} B_{t1} B_n + \frac{1}{\mu} B_{0t1} B_{0n} \\ \frac{m_{t2} m_n}{\varrho} - \frac{1}{\mu} B_{t2} B_n + \frac{1}{\mu} B_{0t2} B_{0n} \\ 0 \\ \frac{m_n}{\varrho} B_{t1} - \frac{m_{t1}}{\varrho} B_n \\ \frac{m_n}{\varrho} B_{t2} - \frac{m_{t2}}{\varrho} B_n \\ \frac{m_n}{\varrho}(E_1 + \frac{B_1^2}{2\mu} + p) - \frac{B_{1n}}{\mu} \\ \times(\frac{m_n}{\varrho} B_{1n} + \frac{m_{t1}}{\varrho} B_{1t1} + \frac{m_{t2}}{\varrho} B_{1t2}) \\ + \frac{B_{1t1}}{\mu}(\frac{m_n}{\varrho} B_{0t1} - \frac{m_{t1}}{\varrho} B_{0n}) \\ + \frac{B_{1t2}}{\mu}(\frac{m_n}{\varrho} B_{0t2} - \frac{m_{t2}}{\varrho} B_{0n}) \\ \frac{\varrho_2}{\varrho} m_n \end{pmatrix}. \tag{51}$$

Eigenvalues and eigenvectors

For the Jacobian matrix of the 9-th component flux function, eigenvalues λ^m, $m = 1, \ldots, 9$ are:

$$\lambda^1 = m_n', \tag{52}$$

$$\lambda^{2,3} = m_n' \pm |B_n'|, \tag{53}$$

$$\lambda^{4,5} = m_n' \pm c_+, \tag{54}$$

$$\lambda^{6,7} = m_n' \pm c_-, \tag{55}$$

$$\lambda^8 = 0, \tag{56}$$

$$\lambda^9 = m_n', \tag{57}$$

with the notation

$$\mathbf{u}'_n = (\varrho, \mathbf{m}'_n, \mathbf{B}'_n, E, \varrho_2)^T = \\ (\varrho, m_n/\varrho, m_{t1}/\varrho, m_{t2}/\varrho, B_n/\sqrt{\mu\varrho}, B_{t1}/\sqrt{\mu\varrho}, B_{t2}/\sqrt{\mu\varrho}, E, \varrho_2)^T. \tag{58}$$

Here, variables with $'$ have a dimension of velocity and $|B'_n|$, c_+ and c_- correspond to Alfvén, fast and slow speeds, respectively. The eigenvectors $\mathbf{r}_m$ which correspond to λ^m are:

$$\mathbf{r}^1 = \begin{pmatrix} 1 \\ m'_n[A \\ m'_{t1} \\ m'_{t2} \\ 0 \\ 0 \\ 0 \\ m'^2/2 \\ 0 \end{pmatrix}, \tag{59}$$

$$\mathbf{r}^{2,3} = \begin{pmatrix} 0 \\ 0 \\ \mp B''_{t2}\cdot sgn(B'_n) \\ \pm B''_{t1}\cdot sgn(B_n) \\ 0 \\ B''_{t2}\sqrt{\frac{\mu}{\varrho}} \\ -B''_{t1}\sqrt{\frac{\mu}{\varrho}} \\ \mp(B''_{t2}m'_{t1} - B''_{t1}m'_{t2})\cdot sgn(B'_n) + (B''_{t2}B'_{1t1} - B''_{t1}B'_{1t2}) \\ 0 \end{pmatrix}, \tag{60}$$

$$\mathbf{r}^{4,5} = \begin{pmatrix} a_f \\ a_f(m'_n \pm c_+) \\ a_f m'_{t1} \mp a_s B''_{t1} c_+ B'_n \\ a_f m'_{t2} \mp a_s B''_{t2} c_+ B'_n \\ 0 \\ a_s B''_{t1} c_+^2 \sqrt{\frac{\mu}{\varrho}} \\ a_s B''_{t2} c_+^2 \sqrt{\frac{\mu}{\varrho}} \\ a_f\cdot 0.5\cdot m'^2 + a_f c_+^2/(\gamma-1) \pm a_f c_+ m'_n \\ \mp a_s c_+ (B''_{t1} m'_{t1} + B''_{t2} m'_{t2}) B'_n \\ +a_f(-1)/(\gamma-1)(c_+^2 - c_0) \\ +a_f(c_+^2 - c_0)(B''_{t1}B''_{1t1} + B''_{t2}B''_{1t2}) \\ /(B''^2_{t1} + B''^2_{t2}) \\ a_f \varrho_2/\varrho \end{pmatrix}, \tag{61}$$

$$\mathbf{r}^{6,7}=\begin{pmatrix} a_s \\ a_s(m'_n \pm c_-) \\ a_s m'_{t1} \pm a_f B''_{t1}\sqrt{c_0}/c_+ \cdot sgn(B'_n) \\ a_s m'_{t2} \pm a_f B''_{t2}\sqrt{c_0}/c_+ \cdot sgn(B'_n) \\ 0 \\ -a_f B''_{t1}\sqrt{\frac{\mu}{\varrho}}c_0/c_+^2 \\ -a_f B''_{t2}\sqrt{\frac{\mu}{\varrho}}c_0/c_+^2 \\ a_s \cdot 0.5 \cdot m'^2 + a_s c_-^2/(\gamma-1) \pm a_s c_- m'_n \\ \pm a_f(B''_{t1}m'_{t1}+B''_{t2}m'_{t2}) \\ \times\sqrt{c_0}/c_+ \cdot sgn(B'_n) + a_s(-1)/(\gamma-1)(c_-^2-c_0) \\ +a_s(c_-^2-c_0)(B''_{t1}B''_{1t1}+B''_{t2}B''_{1t2}) \\ /(B''^2_{t1}+B''^2_{t2}) \\ a_s\varrho_2/\varrho \end{pmatrix}, \tag{62}$$

$$\mathbf{r}^8=\begin{pmatrix}0\\0\\0\\0\\1\\0\\0\\0\\0\end{pmatrix}, \qquad \mathbf{r}^9=\begin{pmatrix}1\\m'_n\\m'_{t1}\\m'_{t2}\\0\\0\\0\\0.5\cdot m'^2\\1\end{pmatrix}, \tag{63}$$

where:

$$B''_{t1}=(B'_{t1}+\epsilon)/(B'^2_{t1}+B'^2_{t2}+2\epsilon^2)^{1/2}, \tag{64}$$

$$B''_{t2}=(B'_{t2}+\epsilon)/(B'^2_{t1}+B'^2_{t2}+2\epsilon^2)^{1/2}, \tag{65}$$

$$a_f=(c_+^2-B'^2_n)^{1/2}/(c_+^2-c_-^2)^{1/2}, \tag{66}$$

$$a_s=(c_+^2-c_0)^{1/2}/(c_+^2-c_-^2)^{1/2}c_+. \tag{67}$$

The symbol ϵ is a small number and c_0 is the sound speed. Then the upwind numerical flux $\underline{\mathbf{F}}_{ij}$ at the interface of control volumes i and j can be written as:

$$\begin{aligned}\underline{\mathbf{F}}_{ij}=\frac{1}{2}[&\mathbf{F}(\mathbf{u}_{1nj},\mathbf{B}_{0nj})+\mathbf{F}(\mathbf{u}_{1ni},\mathbf{B}_{0ni})- \\ &\mathbf{R}_{ij}\,|\,\boldsymbol{\Lambda}_{ij}\,|\,\mathbf{R}_{ij}^{-1}(\mathbf{u}_{1nj}-\mathbf{u}_{1ni})],\end{aligned} \tag{68}$$

where the eigenvector matrix $\mathbf{R}_{ij}$ and the eigenvalue matrix $\boldsymbol{\Lambda}_{ij}$ are calculated from the symmetric average of $\mathbf{u}_{1nj}$ and $\mathbf{u}_{1ni}$. To get a higher-order accuracy, the MUSCL approach is used with indices i and j being replaced by r and l, suffixes which indicate variables just on the left and right sides of the interface [27].

It is noteworthy that a numerical scheme has been developed by Shyue [28] to model multicomponent fluids with the general Mie-Grüneisen equation of state. This scheme combines the Euler's equations of gas dynamics with a set of effective equations for the material-dependent functions.

10. Implementation of the 8-th wave Riemann solver to the problem of magetosonic waves in a coronal loop

This research has been motivated by the new observations of oscillations of coronal loops, detected by the spacecrafts TRACE and SUMER/SOHO, and in the ground-based solar eclipse imaging instrument SECIS [29–31]. They include short period (1-10 s) oscillations which have been observed for several decades in the modulated radio emission, *e.g.* [30], but it is only very recently that they have been observationally identified in the optical band as propagating waves in a coronal loop [32]. These oscillations are only in the SECIS data, TRACE and SOHO do not have this resolution. It is believed that these oscillations are associated with MHD modes of coronal plasma structures and, consequently, thet are an ideal tool for coronal seismology [33, 34], an idea first put forward by Roberts, Edwin and Benz [35]. An understanding of these oscillations is particularly important because they may shed some light on the puzzles of coronal heating and the solar wind acceleration, providing seismic information about the coronal plasma.

The theory of coronal loop oscillations has been developed in some detail for the special case of a straight and infinite cylinder of a magnetic field by Edwin and Roberts [36] who has shown that MHD waves are guided by regions of low Alfvén speed, typically corresponding to regions of high mass density, and thus they are able to form distinctive wave packets. Such regions provide wave guides for fast magnetoacoustic waves. Slow and Alfvén waves are naturally guided along magnetic field lines. In fact the knowledge regarding MHD waves in the solar corona has increased significantly over the last few years. For instance, an extensive investigation of MHD waves in coronal loops has been carried on, *e.g.* [37, 38]. However, the improved resolution of modern observational techniques motivates further development in the study of theoretical aspects of coronal wave activity [30].

A number of theoretical aspects of the study of coronal loop oscillations, connected with the effects of nonlinearity, stratification and 3D structuring remain to be revealed. This subject is devoted to the present studies which are based on numerical modeling of MHD wave processes.

As a consequence of the complexity of MHD waves in highly inhomogeneous coronal plasma it is necessary to understand simpler phenomena which may play the role of elementary building blocks in the construction of a more elaborated theory. As a result, our strategy is to develop simpler models at the initial stage of the research and progressively extend and generalize them to more complex models at subsequent stages. The three-dimensional simulations that we propose in these studies are motivated by the fact that real coronal loops exhibit in fact a multi-dimensional geometry. Traditionally, the studies of kink and sausage modes of a straight magnetic cylinder are performed in the 2.5D geometry. This approach does not allow us to consider linear coupling of various modes, and to model processes of excitation of the modes by an external or asymmetric source. Thus, in this study, we model MHD oscillations of coronal loops with the use of a full-MHD 3D numerical code. Additionally, the 3D simulations allow us to study the effects of excitation.

This paper concerns an infinitely long cylinder of a circular cross section, time-signatures which are made by a wave signal which is collected in time at a fixed

spatial location. The results of numerical simulations will be compared with the earlier results [37, 38] and with the observational data [30]. MHD waves will be excited impulsively inside a coronal loop. In these parametric studies the impulses will possess various spatial profiles. This study is relevant to the case when the wavelength is shorter than the scale height.

We consider the coronal plasma which is described by the following ideal magnetohydrodynamic equations:

$$\frac{\partial \varrho}{\partial t}+\nabla\cdot(\varrho\mathbf{V})=0\,, \tag{69}$$

$$\frac{\partial(\varrho\mathbf{V})}{\partial t}+\nabla\cdot[(\varrho\mathbf{V})\,\mathbf{V}]=-\nabla p+\frac{1}{\mu}(\nabla\times\mathbf{B})\times\mathbf{B}\,, \tag{70}$$

$$\frac{\partial p}{\partial t}+\nabla\cdot(p\mathbf{V})=-p(\gamma-1)\nabla\cdot\mathbf{V}\,, \tag{71}$$

$$\frac{\partial \mathbf{B}}{\partial t}=\nabla\times(\mathbf{V}\times\mathbf{B})\,, \tag{72}$$

$$\nabla\cdot\mathbf{B}=0\,, \tag{73}$$

where ϱ is the mass density, $\mathbf{V}$ is the flow velocity, $\mathbf{B}$ is the magnetic field, p is the pressure, μ is the magnetic permeability, and $\gamma=5/3$ is the adiabatic index.

As in a realistic model of a coronal loop, a number of effects crowd in and complicate our understanding of the wave phenomena we assume a simple coronal loop model. In this way, we consider briefly some of the effects that require evaluation, if we are to explain the observed wave signatures in coronal loops. We enquire what effects are most likely important, and we try to estimate the time-scales which they produce.

In the model we discuss, a magnetically structured atmosphere in which the magnetic field is uniform and directed in the z-direction. We ignore the effects of gravity, field line curvature, twisted loops, non-circular cross-sections and approximate the coronal loop by smooth plasma profiles in which the inhomogeneity occurs in the r-direction, and the ϕ-direction is perpendicular both to the r- and z-directions.

In particular, we consider a loop of a cross-section radius a, field strength B_0 and mass density ϱ_0 embedded in a magnetic environment with field strength B_e and mass density ϱ_e. The mass density $\varrho_0(r)$ profile is chosen as [38]:

$$\varrho_0(r)=\varrho_e+(\varrho_i-\varrho_e)\,\mathrm{sech}^4\left(\frac{r}{a}\right)\,, \tag{74}$$

where a is the loop radius, indices i and e denote quantities inside the loop and outside the loop, respectively. The equilibrium magnetic field $B_0(r)\hat{\mathbf{z}}$ and pressure $p_0(r)$ profiles must satisfy the total pressure balance condition:

$$\frac{d}{dr}\left(p_0(r)+\frac{B_0^2(r)}{2\mu}\right)=0\,. \tag{75}$$

Hence, at the equilibrium the total (gas plus magnetic) pressure has to be constant. In particular, the total pressure inside the coronal loop is equal to the total pressure outside the coronal loop, *i.e.*:

$$p_i+\frac{B_i^2}{2\mu}=p_e+\frac{B_e^2}{2\mu}. \tag{76}$$

We adopt the magnetic field profile which corresponds to an open magnetic structure, *viz.*:

$$B_0(r) = B_e + (B_i - B_e)\,\mathrm{sech}^4\left(\frac{r}{a}\right) \tag{77}$$

and the expression for $p_0(r)$ follows then from Equation (75).

Similarly as in [38] we specify the plasma β, density ratio d, and the ratio of Alfvén speeds v as:

$$\beta \equiv \frac{2\mu p_e}{B_e^2}, \quad d \equiv \frac{\varrho_i}{\varrho_e}, \quad v \equiv \frac{c_{Ae}}{c_{Ai}}, \tag{78}$$

where $c_{Ae} = B_e/\sqrt{\mu\varrho_e}$ and $c_{Ai} = B_i/\sqrt{\mu\varrho_i}$. Henceforth, we choose and hold fixed

$$d = 3.89, \quad v = 2, \tag{79}$$

which gives us the plasma $\beta = 0.003$.

10.1. Numerical model

MHD Equations (69)–(73) are solved numerically by using the FLASH code [39] which is a nice tool for solving MHD equations numerically. The high-order Riemann solver of a Roe type that is implemented in this code yields accurate results near steep gradients and moving contact discontinuities. The MHD part is implemented with using the Powell's method [20] which allows the divergence of magnetic field to be kept free to machine dependent round-off errors. The computer code is formally second-order accurate in space and time.

The plasma equations are solved numerically on an $x-y-z$ Eulerian box with the dimension $(-10\mathrm{a}, 10\mathrm{a}) \times (-10\mathrm{a}, 10\mathrm{a}) \times (-10\mathrm{a}, 10\mathrm{a})$. For most numerical runs 36 (18) the blocks have been chosen in the x, y (z) directions. The maximum refinement level has been specified as 8. We apply free-boundary conditions at the boundaries of the simulation region. This choice of boundary conditions is a consequence of an extension of the real medium. In this way, we assume that MHD waves have no time to travel the entire length of the loop and they have not reached the ends of the loop, where line-tying in the dense lower atmosphere causes reflection, and so the wave propagates freely as if the structure were open.

10.2. Impulsively generated MHD waves

Let us consider coronal plasma which is modeled by Equations (74) and (77). Perturbations which are excited in the solar corona are very complex. Here, we focus our attention on three separate cases which correspond to impulsively excited waves. Such excitation may be due to a flare or any other sudden release of an energy process.

Introducing normalized variables, we shall measure plasma velocities in units of c_{Ae}, the spatial variables in a and the time in units of the Alfvén transit time $t_A = a/c_{Ae}$.

10.2.1. Slow wave

One of the simplest conceivable models is the case when a slow magnetosonic wave is initially present in the medium. Such wave can be effectively excited by setting the following initial condition:

$$V_z(r, \phi, z, t = 0) = \frac{V_{z0}}{\cosh^2\left(\frac{r}{a}\right)\cosh^2\left(\frac{z}{a}\right)}, \tag{80}$$

$$V_r = V_\phi = 0\,, \tag{81}$$

where we choose the pulse amplitude $V_{z0} = 0.005$.

The initial profile of Equations (80)–(81) excites oscillations in the perturbed mass density profile:

$$\delta\varrho \equiv \varrho - \varrho_0\,, \tag{82}$$

which is shown in the top panel of Figure 1 at $t = 80$. As a result of the initial impact, the region above the initial pulse is compressed while the region $z < 0$ is rarefied. These profiles are symmetric around the z-axis.

The above presented slow wave exhibits time-signatures which are made by collecting wave signals in time at the detection point. As the slow pulse does not experience any significant dispersive distortion, it preserves the information about the initial pulse and we choose the detection point on the loop axis at $z = 4$.

It has been shown by Roberts [35] that slow waves propagate with a speed which is greater than c_{ti} and lower than c_{si}. Here, c_{si} is the sound speed inside the coronal loop and c_{ti} is the so-called tube speed inside the coronal loop:

$$\frac{1}{c_{ti}} = \sqrt{\frac{1}{c_{si}^2} + \frac{1}{c_{Ai}^2}}. \tag{83}$$

Thus, the speed c_{ti} is sub-sonic and sub-Alfvénic. For the low β plasma conditions, c_{ti} is close to the sound speed inside the loop. It follows from the equilibrium conditions that:

$$\frac{c_{si}^2}{c_{Ae}^2} = \frac{\gamma}{2}\frac{(\beta+1)v^2 - d}{dv^2}. \tag{84}$$

For a choice of the equilibrium parameters given by Equation (79), we have:

$$\frac{c_{si}}{c_{Ae}} \approx 0.077. \tag{85}$$

Thus the slow wave should reach the detection point $r = 0,\ z = 4$ at $t \approx 52$ in good agreement with Figure 1 (bottom panel).

Slow and fast magnetoacoustic waves are coupled, while in this case the Alfvén wave decouples from the magnetosonic waves and therefore it is absent in the system. As a consequence of this coupling, the fast wave must be present in the system, being driven by the slow magnetosonic wave. However, the fast wave is of the amplitude 10^{-5} that is much lower than the slow wave amplitude. As a consequence of that, such a small wave would be hardly detectable in the real system which always contains a noisy background. Hence, this wave is insignificant and therefore it is not shown.

10.2.2. Fast sausage wave

In this case we initially launch a pulse of the form:

$$V_r(r,\phi,z,t=0) = \frac{V_{0r}\, r}{\cosh^2\left(\dfrac{r}{a}\right)\cosh^2\left(\dfrac{z}{a}\right)}\,, \tag{86}$$

$$V_\phi = V_z = 0\,. \tag{87}$$

Here $V_{0r} = 0.005$ is a pulse amplitude. This pulse basically excites fast sausage waves which correspond to symmetric pulsations of the loop, with the central axis of this loop remaining undisturbed. In particular, the radial component of plasma

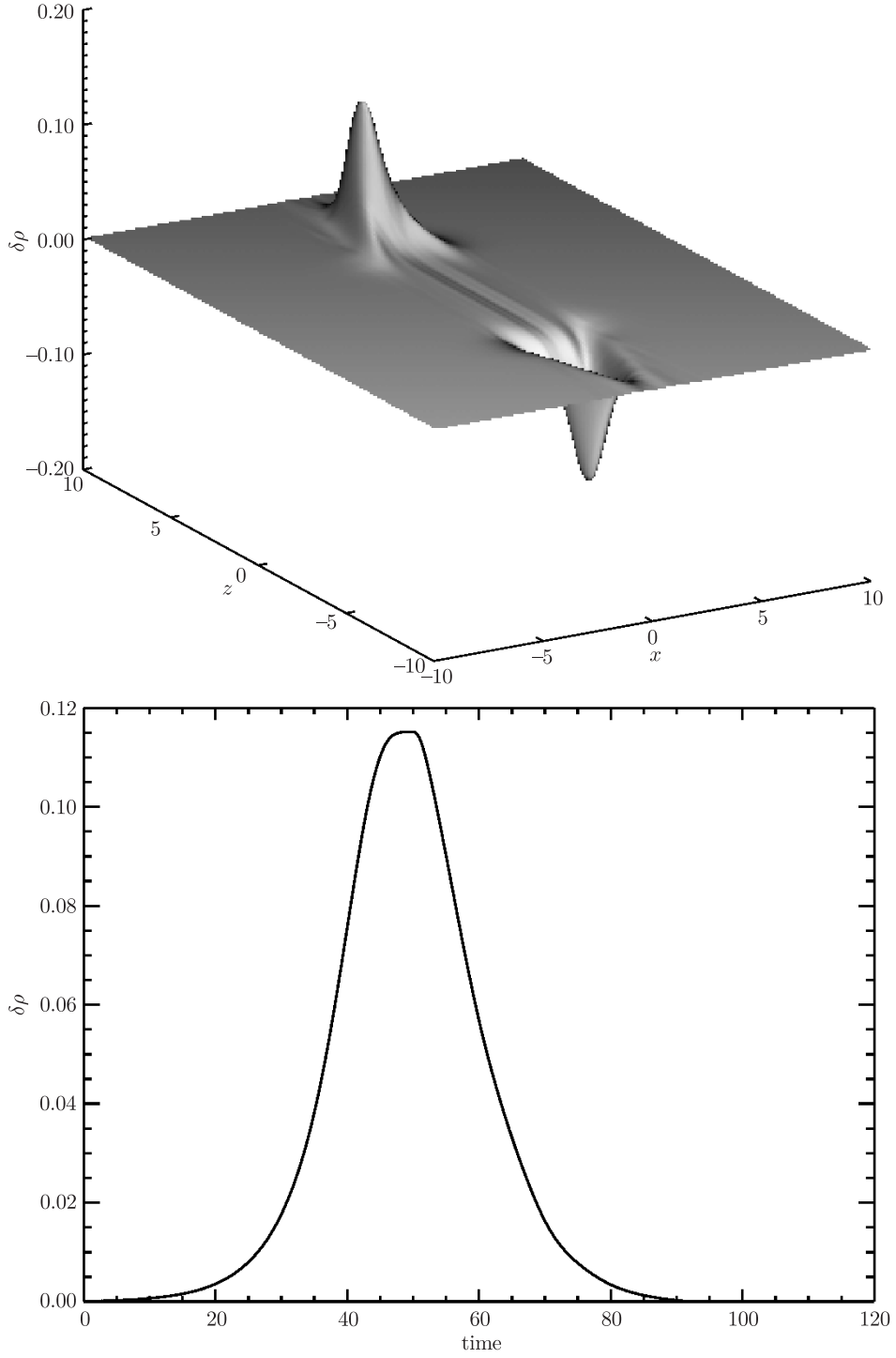

Figure 1. The spatial profile of the perturbed mass density $\delta\varrho(x, y = 0, z, t = 80)$ (top panel) and the time-signature which is obtained by measuring the wave signal in $\delta\varrho$ at $x = y = 0$, $z = 4$: V_z (bottom panel) in the case of the initially launched pulse of Equations (80)–(81) which corresponds to an essentially slow wave

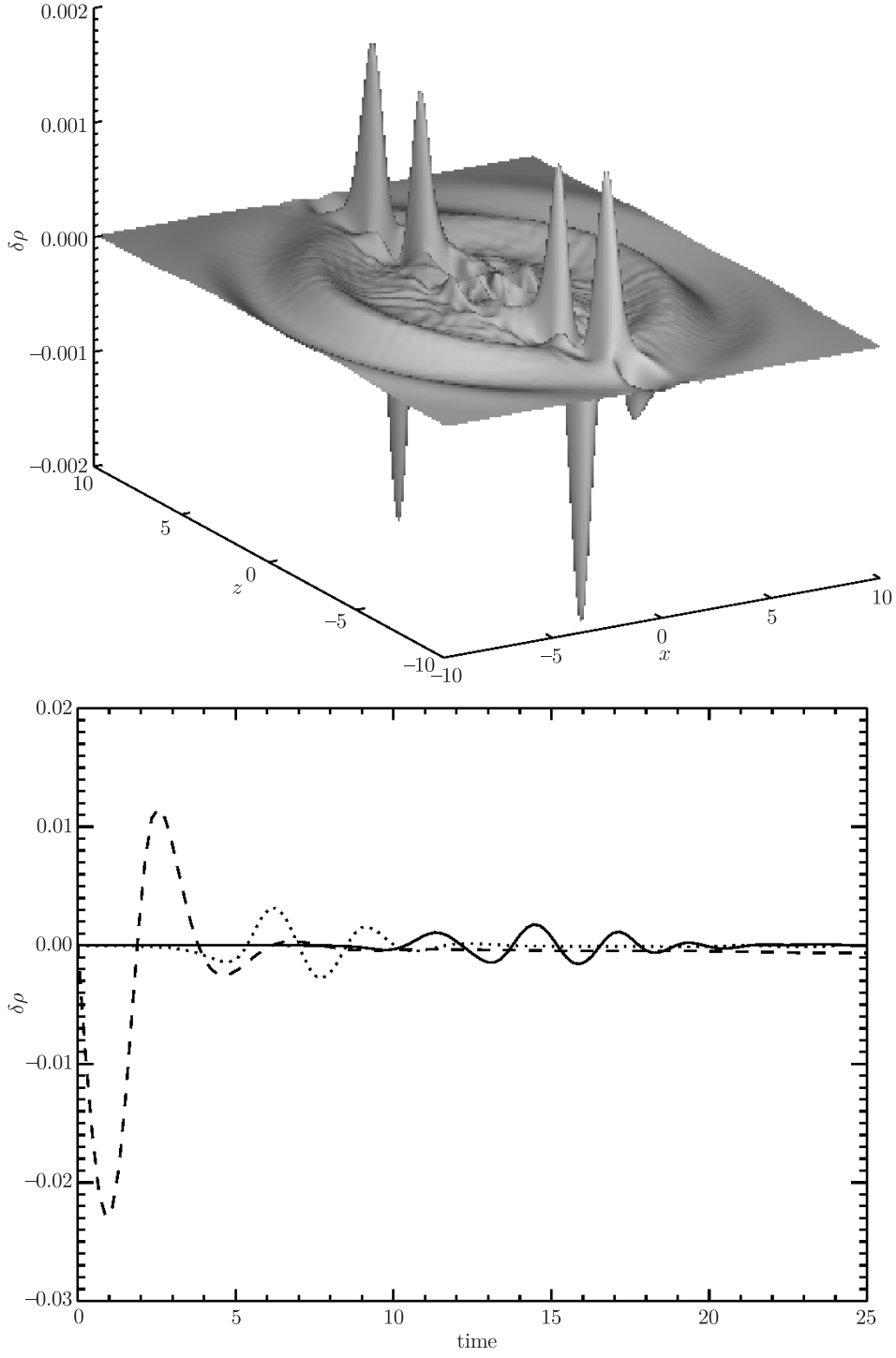

Figure 2. The spatial profile of $\delta\varrho(x,y=0,z,t=9)$ (top panel) and a time-signature which is obtained by measuring the mass density at the detection point $x=y=0$, $z=0$ (dashed line), $z=4$ (dotted line), and $z=9$ (solid line) (bottom panel) in the case of the initial conditions (86)–(87) that corresponds to a fast sausage wave

motions disappears at this axis and it changes the sign at $r=0$. This wave is unable to propagate for a sufficiently long wavelength as it leaks energy outside the loop. This leakage is represented by the circular wave patterns in the top panel of Figure 2 which displays the spatial profile of $\delta\varrho$ at $t=9$. This profile corresponds to a fast sausage mode and it is symmetric around the z-axis. The Alfvén wave is absent in the system as it decouples from the magnetosonic waves.

Time-signatures that are associated with the fast sausage wave are shown in Figure 2 (bottom panel). It should be noted that the fast sausage wave exhibits short-period oscillations, the scenario which is quite different than in the case of the slow wave of Figure 1 (bottom panel). These few-seconds oscillations are a result of the fact that sausage modes are more dispersive than a slow wave and the former ones are leaky for sufficiently long wavelength oscillations. As a consequence of that only short oscillations are guided along the coronal loop.

10.2.3. Fast kink wave

A simple way to excite a fast kink wave in the system is to launch the following pulse:

$$V_x(r,\phi,z,t=0)=\frac{V_{x0}}{\cosh^2\left(\frac{x-x_0}{a}\right)\cosh^2\left(\frac{y}{a}\right)\cosh^2\left(\frac{z}{a}\right)}, \tag{88}$$

$$V_y=V_z=0\,, \tag{89}$$

where $V_{x0}=0.005$ is the pulse amplitude and x_0 is its initial position. This pulse excites a packet of waves in which the highest contribution has a fast kink wave. A pure kink wave involves lateral displacements of the loop, maintaining a circular cross-section, with the axis of the loop resembling a wriggling snake. We may view this as a global mode of an oscillation of a coronal loop, moving the whole loop in its vibration. This mode exists for all wavelengths as a trapped oscillation of the loop. Obviously, the radial component of plasma motions at the loop center, $r=0$, generally differs from zero, $V_r\neq 0$.

Roberts [35] show that the kink mode moves at a speed c_k which is determined by both c_{Ae} and c_{Ai}; the kink mode speed is greater than c_{Ai} and lower than c_{Ae}. In the long wavelength limit ($\lambda\gg a$), the phase speed of the principal kink wave is given by the kink speed c_k [35] such that:

$$c_k=\sqrt{\frac{\varrho_i c_{Ai}^2+\varrho_e c_{Ae}^2}{\varrho_i+\varrho_e}}. \tag{90}$$

This speed is the mean Alfvén speed of the medium, intermediate between the Alfvén speed inside the loop and the Alfvén speed in the ambient medium. It is interesting that c_k is closer to c_{Ai}, particularly for shorter waves. Consequently, the kink wave reaches the detection point ($r=0,\ z=4$) at $t\approx 8$ in a good agreement with Figure 3. This figure shows a signal in B_x as the perturbed mass density profile is of a low magnitude and therefore it is not displayed.

Now, we will discuss the case of the initial pulse of Equations (88)–(89) with $x_0=-10$. Such pulse produces complex time-signatures. Indeed, Figure 4 shows time-signatures which are made by collecting the perturbed mass density at three spatial points: (a) (0,0,0) (dashed line); (a) (0,0,4) (dotted line); (a) (0,0,9) (solid line). It

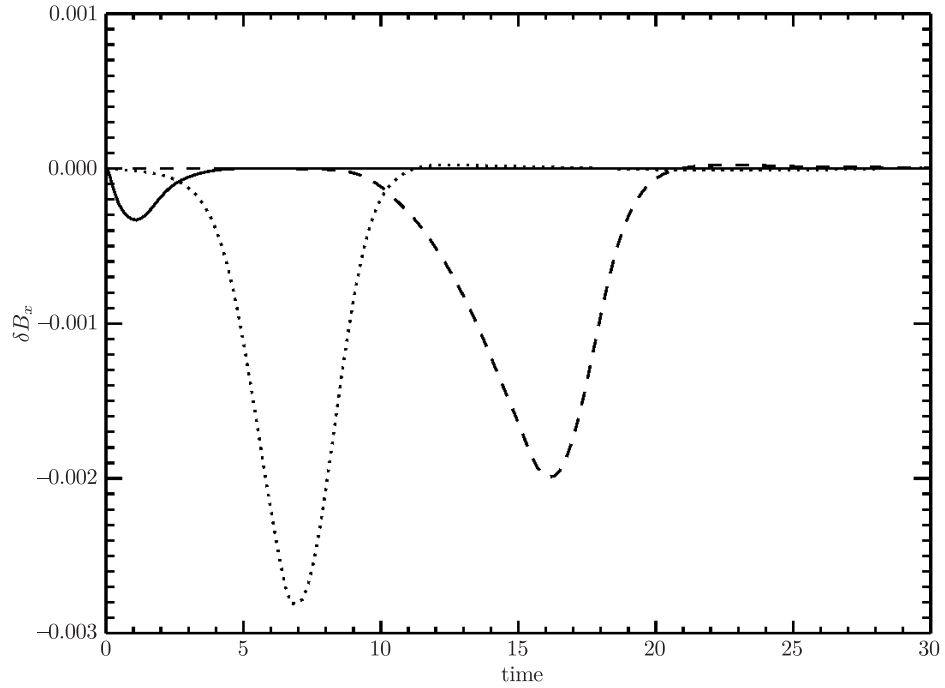

Figure 3. Time-signatures which are obtained by measuring appropriate signals in δB_x at the detection point $x = y = 0$, $z = 0$ (dashed line), $z = 4$ (dotted line), and $z = 9$ (solid line) in the case of the initial conditions (88)–(89) with $x_0 = 0$

is discernible that the time-signatures are more complex with a larger distance from the exciter.

As the fast and slow waves are coupled we expect a signal being present in the longitudinal component of velocity, V_z. Obviously, this signal is of a lower magnitude that the signal in V_x (not shown). In this case, the initial condition (89) excites also a signal in V_ϕ which corresponds to the Alfvén wave (not shown).

10.3. Concluding remarks

We have developed a simple model of the coronal plasma. This model makes no allowance for loop curvature, stratification, nor is there any realistic modeling of the coupling of the coronal plasma to the denser layers of the solar atmosphere. With a use of this model, we have numerically simulated the coronal plasma's response to the impulsively generated MHD waves. We have adapted the FLASH code [39] which is based on the Godunov-type method, *e.g.* [40]. In the Godunov method [2] the interaction of a pair of numerical cells at their interface is assumed to take place through a number of waves [41]. This yields an accurate scheme which avoids non-physical oscillations in the vicinity of shock waves.

The primary result of the study reported on here is the demonstration of the importance of the exciting conditions on the propagation of the magnetosonic waves. Our results both complement and extend those of the earlier published studies, and we have attempted to clarify some of the subtler aspects of the wave theory. By such

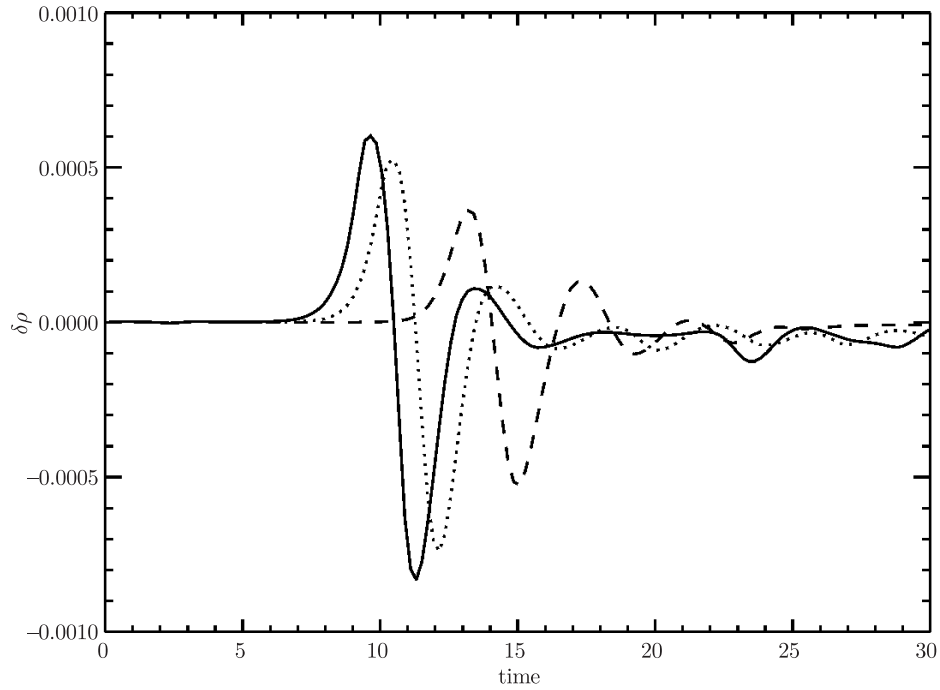

Figure 4. The time-signature which is obtained by measuring the mass density at the detection point $x = y = 0$, $z = 0$ (solid line), $z = 4$ (dotted line), and $z = 9$ (dashed line) which are generated from the initial conditions (88)–(89) with $x_0 = -10$

approach we might embrace the important physical processes of oscillations studied in geophysics, oceanography, atmospheric, and astrophysical contexts.

A slow pulse (V_z) is associated with a relatively strong perturbations of the mass density. A fast sausage pulse (V_r) does not lead to localized perturbations of the mass density in the loop. This is a consequence of the fact that short waves are trapped by the loop while long waves are leaky. An infinitely long kink wave can oscillate in a loop but when the initial pulse is located on the loop axis it does not perturb significantly a mass density. On the other hand, the external pulse leads to mass density alterations which lead to complex time-signatures.

11. The implementation of the 9-th wave Riemann solver to the problem of solar wind interaction with Venus

The planet Venus has been the subject of intense investigation since Mariner 2 flew by the planet in the fall of 1962. Observations of Venus by orbital missions have led to a significant improvement of our knowledge about the upper atmosphere and ionosphere of Venus and their interaction with the solar wind. Since the internal magnetic field of Venus is negligibly small or even nonexistent, the solar wind interaction with Venus differs from their terrestrial counterparts. This lack of a magnetic field allows the solar wind to make direct contact with the ionosphere of the planet.

Pioneer Venus Orbiter (PVO) as well as other spacecraft observations have revealed that the solar wind interaction with Venus leads to a highly structured plasma, *e.g.* [42]. As a result of supersonic and superalfvénic solar wind flow, a *bow*

shock forms upstream of the planet. The shock slows, heats, and also assists in deflecting the solar wind. The shock which is a standing fast magnetosonic wave for average solar wind conditions departs from the obstacle so that the plasma that crossed the shock can flow around the planet. The bow shock size depends on the solar wind Mach numbers, solar wind dynamic pressure as well as on the shape and size of the ionosphere [43]. Apparent asymmetries in the shock shape result from the interplanetary magnetic field which is oblique to the solar wind flow (IMF) [44].

Downstream of the bow shock is a sharp gradient in the electron density known as *ionopause*. This is a region which separates the shocked and magnetized solar wind plasma from the thermal ionospheric plasma. The ionopause forms the surface of Venus at the altitude above where the ionospheric gas pressure is approximately balanced by the incident pressure in the overlaying magnetic barrier. The ionopause was observed to be typically located at about 300 km in the subsolar region and about 1000 km near the terminator [42]. It is generally accepted that the height of the terminator ionopause affects the transport of ionospheric plasma to the nightside. On the occasion when the solar wind dynamic pressure is high enough to substantially lower the terminator ionopause altitude, the nightside ionosphere observed by PVO is found to be highly depleted [45, 46]. This phenomenon is called the disappearing ionosphere.

The region between the bow shock and the ionopause is referred to as the *magnetosheath* [42]. The magnetosheath by itself contains a region (close to the ionopause) of enhanced magnetic pressure referred to as the *magnetic barrier* [47].

It is well known that Venus has a dayside exosphere which is dominated by oxygen at altitudes above 400 km from the planetary surface. The *ionosphere* is a partially-ionized component of exosphere above about 140 km from the surface of Venus. This region contains electrons and various ion species such as O^+, H^+, O_2^+, CO_2^+, and others. The ionosphere is approximately in photochemical equilibrium below an altitude of about 200 km at Venus for all ions. Above 200 km, O^+ becomes the major ion in this region. The principal ionization source on the dayside is provided by solar photoionization of thermospheric gases such as O by solar extreme ultraviolet (EUV) radiation, although other ionization processes such as impact ionization and charge exchange may also contribute in a major way. On the nightside, solar photoionization does not contribute directly to the ionization, and the maintenance of the nightside ionosphere requires ion transport from the dayside through the terminator. The nightward ion flow is driven primarily by the large pressure gradient at the terminator. The ion flow generally increases with the solar zenith angle (SZA), reaching values larger than 7 km/s downstream of the terminator [48]. Ion-neutral chemical reactions and electron-ion charge exchange are both important processes in the lower ionosphere.

The observations of the nightside ionosphere have provided evidence that the ionospheric plasma is highly structured and dynamic, *e.g.* [49], often exhibiting large-scale structures which are called *tail rays*. The ionosphere has a tendency to form a central tail ray, often with rays on either side, to the north and south. The rays have dimensions of the order of $1–3 \cdot 10^3$ km, decreasing in width at higher altitudes [50]. Although the downstream extent of these structures has not been measured

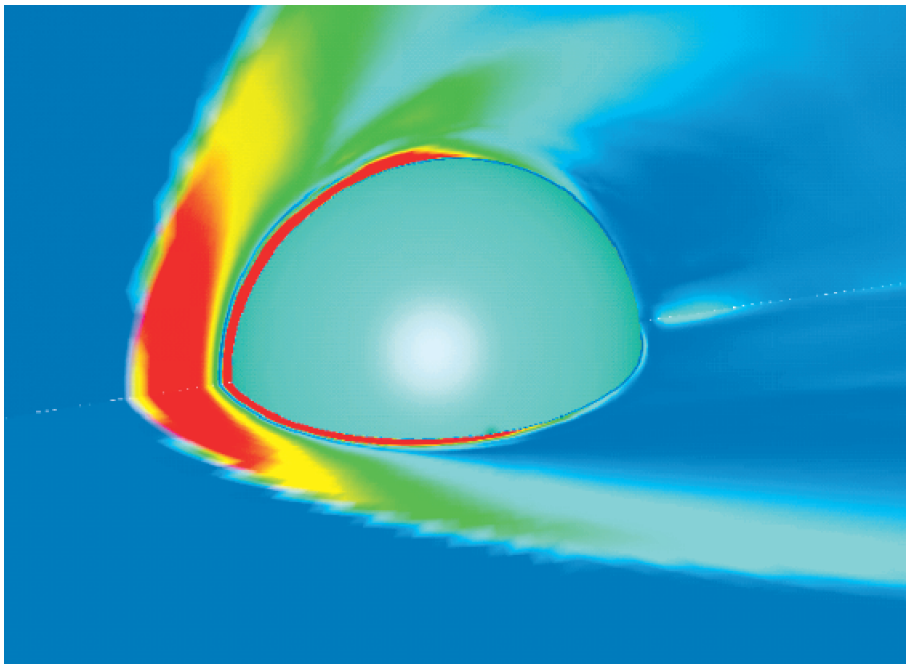

Figure 5. Pressure distribution around Venus. The equatorial and meridian planes are horizontal and vertical, respectively

since spacecraft orbits crossed them almost horizontally, it is supposed that they must extend tailward at least a few thousand kilometers downstream.

In the nightside ionosphere, there are also regions of mass density depletions referred to as *ionospheric holes* [51]. The density in these holes is lower than in the surrounding ionosphere by up to two orders of magnitude. The plasma in the holes differs from that found in their surrounding; H^+ becomes a major ion in the holes, while O^+ is the major ion outside. These holes are associated with a strong magnetic field which points tailward [52].

Most recent numerical simulations of the three-dimensional interaction between the solar wind and Venus have largely improved our understanding of the large scale physical processes [4, 5, 26, 53, 54]. In particular, Murawski and Steinolfson [4] included mass loading due to photoionization of the oxygen atoms and showed that the solar wind was decelerated by the mass loading and the bow shock is pushed farther outward from the planet. However, this model was developed for the case when the IMF was parallel to the solar wind flow, simplifying the geometry to two dimensions. This model was extended to three dimensions by Murawski and Steinolfson [5] and the case of the IMF perpendicular to the solar wind flow was considered. In another model, solar wind interaction with the ionosphere of Venus was numerically simulated in the framework of two-component, three-dimensional MHD model by Tanaka and Murawski [26]. This model is briefly described here. The effect of a decreased ionospheric pressure which occurs under the condition of a high speed solar wind or a low solar extreme ultraviolet (EUV) flux, was discussed by Tanaka [54, 55]. The results of numerical simulations showed that the IMF penetrated

from the magnetosheath to the dayside ionosphere so as to increase the ionospheric total pressure.

The purpose of this subsection is to demonstrate that the basic features of the solar wind interaction with the ionosphere of Venus can be reproduced by applying a two-component MHD model which was developed by Tanaka and Murawski [26] and Tanaka [54, 55]. This subsection is organized as follows. A numerical model of the solar wind and ionospheric plasma dynamics is reviewed in Section 11.1. The numerically obtained results and the discussion are presented in the following section. This subsection closes with some concluding remarks.

11.1. Numerical model

We assume that the neutral atmosphere of Venus consists of oxygen atoms and of the carbon dioxide molecules both of which are stratified gravitationally. Their number densities at the lower boundary of the atmosphere are $10^{10}\,\mathrm{cm}^{-3}$ and $5\cdot10^{10}\,\mathrm{cm}^{-3}$, respectively. The peak number densities occur at an altitude of 140 km above the planetary surface, in agreement with the PVO observations [56]. The ionosphere is approximately in photochemical equilibrium at lower altitudes. O^+ ions are produced primarily by the solar EUV incident on the neutral atmosphere, $O+h\nu\rightarrow O^+$, and by charge exchange with CO_2^+ ions, $CO_2^+ + O\rightarrow O^+ + CO_2$. These chemical reactions occur with the production rates $q_1 = 10^{-10}\,(\mathrm{cm^3 s})^{-1}$ and $q_2 = 10^{-10}\,(\mathrm{cm^3 s})^{-1}$, respectively. The density of CO_2^+ ions is calculated from the photo-chemical equilibrium. O^+ ions experience some losses during their charge exchange with molecules of the carbon dioxide, *viz.*, $O^+ + CO_2 \rightarrow CO + O_2^+$. The loss rate for O^+ ions is $L_1 = 9.4\cdot10^{-10}\,(\mathrm{cm^3 s})^{-1}$.

CO_2^+ ions are produced by the photoionization of the carbon dioxide molecules, $CO_2 + h\nu \rightarrow CO_2^+$, and they experience charge losses during a chemical reaction with the oxygen atoms, *viz.*, $CO_2^+ + O \rightarrow O_2^+ + CO$. The loss rate for CO_2^+ ions is $L_2 = 1.64\cdot10^{-10}\,(\mathrm{cm^3 s})^{-1}$.

We assume that the solar wind plasma consists of H^+ ions which the flow with the same velocity as O^+ ions. The set of equations used for a description of the solar wind interaction with Venus is that of two-component, ideal MHD that includes mass production and loss terms in the mass continuity equation, and aeronomical collision and gravity terms in the momentum equation. We solve the following set of MHD equations as an initial value problem:

$$\mathbf{u}_{,t} + \mathbf{F}_{,x} + \mathbf{G}_{,y} + \mathbf{H}_{,z} = \mathbf{S}. \tag{91}$$

Here, the state vector of nine dependent variables is:

$$\mathbf{u} = (\varrho, m_x, m_y, m_z, B_x, B_y, B_z, E, \varrho_2)^T \tag{92}$$

and $\mathbf{F}$, $\mathbf{G}$, and $\mathbf{H}$ are flux functions in the x, y, and z directions [54, 55], respectively.

The source term $\mathbf{S}$ depends on the ion production due to photoionization and ion-neutral chemistry, q_1, q_2, as well as on losses due to ion-neutral reactions, L_1, L_2 (H^+ ion-electron recombination is neglected in this model), *viz.*:

$$\begin{aligned}\mathbf{S} =& (q_1+q_2-L_1-L_2, -\nu\mathbf{m}-\varrho\mathbf{g}, 0, 0, 0,\\ & -\frac{\mathbf{m}}{\varrho}\cdot(\nu\mathbf{m}+\varrho\mathbf{g}) + \frac{T_q}{\gamma-1}(q_1+q_2) - \frac{T_L}{\gamma-1}(L_1+L_2), q_2-L_2)^T.\end{aligned} \tag{93}$$

In the above formulae, ϱ is the total ion density, $\varrho = \varrho_1 + \varrho_2$, with ϱ_1 and ϱ_2 corresponding to H^+ ions and O^+ ions, respectively. The symbol $\mathbf{m} \equiv \varrho \mathbf{V} = (m_x, m_y, m_z)$ denotes the momentum. $\mathbf{B}$ is the magnetic field. E is the total energy density. ν is the ion-neutral drag collision frequency. The ratio of specific heats is $\gamma = 5/3$. $T_q = 10^3$ K is a production temperature of photoions and T_L is a loss temperature due to a chemical reaction of the O^+ ions with the carbon dioxide. The other terms in the expressions above are self-explanatory.

We assume that the magnetic field is perpendicular to the solar wind flow, while the IMF is typically oriented about 42° from the Sun-Venus line in the proper sense for an Archimedean spiral [57]. As the perpendicular magnetic field case is simpler than the oblique field case, the present simulations will provide an insight into the more complex case. Consequently, the perpendicular magnetic field case seems to be motivated.

Equation (91) is solved in all three spatial dimensions of a spherical r, θ, ϕ coordinate system by adopting a finite-volume method which uses a TVD scheme which was already successfully applied for a single-component plasma [17, 27, 58]. The size of the Jacobian matrix for Equation (91)increases to 9×9 from 8×8 for one-component MHD equations [55]. The eigen-value problem for this Jacobian consists of two Alfvén, two fast, two slow, and two entropy waves. Consequently, there is one more entropy wave in comparison to the eigen-waves of the Jacobian of the one-component MHD equations. Details of the present approach can be found elsewhere [26, 55].

The inner and outer boundaries of the simulation region are set at about 1 R_p and 10 R_p, respectively. Here $R_p = 6053\,\mathrm{km} + 140\,\mathrm{km}$ is the planetary radius. While the inflow boundary conditions are maintained on the dayside of the outer boundary, the zero-gradient boundary conditions are adopted on the downstream side. The ion-neutral collision and ion chemical processes become dominant near the inner boundary. Therefore, an ion chemical equilibrium and zero plasma velocity conditions are adopted at the inner boundary. The ion temperature is fixed and held constant at the inner boundary throughout the simulation process.

The simulation code used a $88 \times 80 \times 86$ grid points along $r \times \theta \times \phi$ directions. This grid provides angular grid spacings $\Delta\theta = 4.5°$ and $\Delta\phi \simeq 4°$. The radial grid was chosen nonuniform with a finest grid of $0.00025\,R_p$ at the inner boundary of the simulation region. The coarsest grid of $0.33\,R_p$ was set at the outer boundary.

A typical computation begins with the introduction of the desired solar wind values in the dayside within the numerical box. The numerical solution continues then until the interaction process achieves an approximate steady state.

11.2. Numerical results and discussion

We report here only some of the results from our simulations. More details can be found in Tanaka and Murawski [26] and Tanaka [55]. We present all numerical results for the following solar wind parameters: proton density $n_e = 14\,\mathrm{cm}^{-3}$, temperature $T = 10^5$ K, sound speed 61 km/s, solar wind speed 311 km/s which gives sonic Mach number 5.1, the plasma $\beta = 0.6$, and the magnetic field strength 15 nT. These parameters correspond to the maximum of solar activity [59].

Figure 6 shows the pressure profiles along the Sun-Venus line. In the upstream solar wind, kinetic pressure ϱV^2 dominates gas pressure p and magnetic pressure

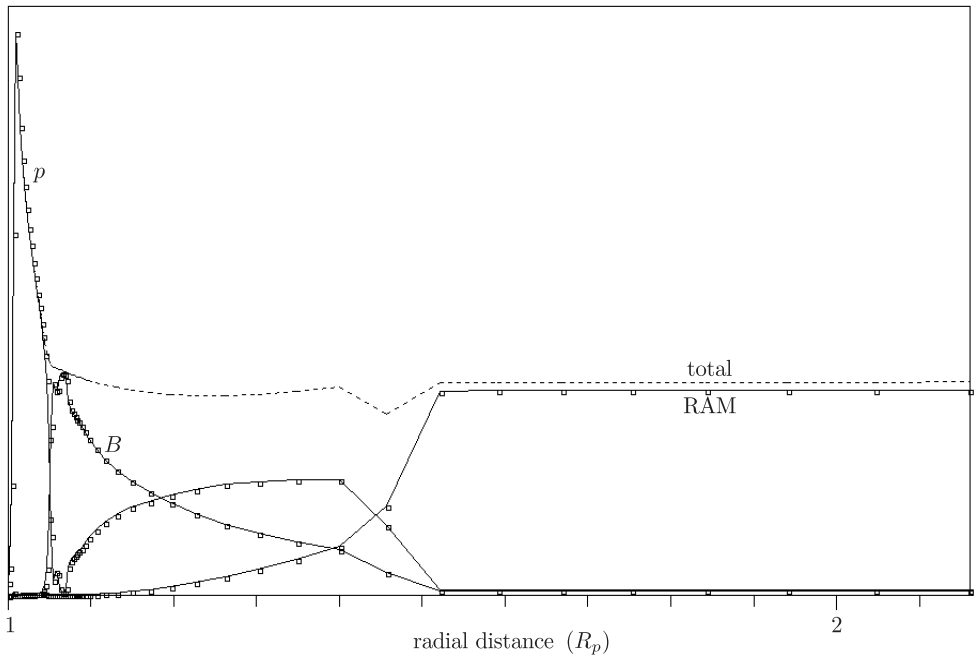

Figure 6. The distributions of the gas pressure p, the magnetic pressure p_B, and the dynamic pressure ϱV^2 along the Sun-Venus line on the subsolar side. The horizontal axis shows the radial distance normalized to the planet radius R_p and the vertical axis shows relative pressure values. The bow shock at the distance 0.45 R_p, the ionopause at the altitude about 0.04 R_p, and the magnetic barrier which corresponds to the maximum of the magnetic pressure should be noted

$B^2/(2\mu)$. At the bow shock, kinetic energy of the solar wind is converted into thermal energy. As a consequence of that, the gas pressure dominates over the kinetic pressure downstream the bow shock. The distance between the bow shock and the planetary surface is about $0.45\,R_p \simeq 2700\,\mathrm{km}$, where $R_p \simeq 6053\,\mathrm{km}$ is the radius of Venus (Figure 6). With a distance closer to the planetary surface, the magnetic pressure accommodates itself as a result of competitive ionospheric gas pressure, while the gas pressure decreases at the same time. This behavior is a consequence of the magnetic barrier formation whose location corresponds to the magnetic pressure maximum (Figure 6). The magnetic barrier is supported by the gas pressure of cold ionospheric plasma. This pressure is maintained by ionization and ion chemical processes in the planetary upper atmosphere. At the bottom of the ionosphere, the gas pressure is provided by the neutral atmosphere which is lying below through ion-neutral collisions.

The ionopause occurs at the place where the impacting solar wind pressure is balanced by the ionospheric pressure. It is seen in Figure 6 that the dynamic pressure is negligibly small downstream the bow shock, as at the bow shock, the supersonic solar wind flow is diverted into a subsonic flow. Therefore, the ionopause is placed at the point where the gas pressure equals the magnetic pressure, at the distance of about $0.04\,R_p \simeq 240\,\mathrm{km}$ from the planetary surface. The altitude at which the ionopause is located is smallest at the nose, and it grows monotonically with the increasing SZA,

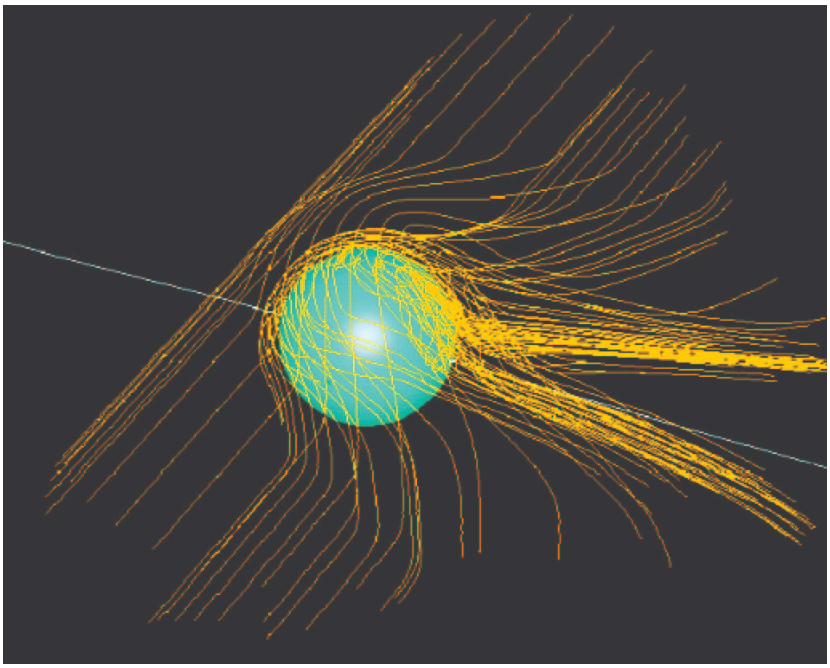

Figure 7. Draping of magnetic field lines around Venus

reaching the largest altitude at the terminator. The ionopause altitude is about $1\,R_p$ at the terminator [26].

Figure 7 shows the global configuration of the the magnetic field lines and plasma density from the final configuration of the numerical simulations. The view is from the tailside. The solar wind flows in from the left-hand side toward the planet. The brown lines indicate magnetic field lines which pile up at the bow shock, and then slip over the ionosphere, forming a magnetotail. Having been dragged through the polar regions the magnetic field lines are convected equatorward by the field line tension and the solar wind flow toward the antisolar direction. The magnetic field geometry on the nightside is related to the draping of the solar wind magnetic field over the obstacle on the dayside. A part of the draped magnetic field apparently sinks into the wake of the planet to create lobes-like structures with sunward and anti-sunward directed magnetic fields.

11.3. Concluding remarks

We have considered the solar wind's interaction with the ionosphere of Venus using numerical solutions of the two-component, three-dimensional MHD equations. The solar wind for these solutions consists mainly of H^+ ions, while the ionosphere's primary component consists of O^+ ions. Loss effects due to the interaction of O^+ ions with molecules of the carbon dioxide are introduced. Such modeling has generally been successful in reproducing the characteristics of the solar wind interaction with Venus.

The main results are the following: The solar wind interaction with Venus leads to the formation of the bow shock and an ionosphere which consists of cold, low speed, weakly magnetized O^+ ions. The ionosphere exhibits a blunt conic shape, with

a highly structured ionotail. The ionotail is flattened with the growing distance from the planetary surface, and the flattening is believed to be due to magnetic field tension forces.

The present results can in principle be applied to any unmagnetized body that has an ionosphere. In particular, the results are expected to be quite relevant to Mars, *e.g.* [60], several comets, *e.g.* [38], and a moon of Saturn – Titan, *e.g.* [61].

12. Summary

This paper presents Godunov-type methods for wave propagation in fluids. Although this presentation is far from complete the emphasis is on the methods which are the most effective and best known methods for the author.

There are several conditions that numerical schemes should satisfy: the accuracy and speed of numerical simulations, adequate representation (without generation of spurious oscillations) of complex flows and steep profiles, as well as *robustness* of the numerical code. A computer code is described as being robust if it has the virtue of giving reliable results to a wide range of problems without needing to be retuned. Modern numerical schemes such as shock-capturing schemes described in this paper satisfy these conditions.

The existing numerical models demonstrate the feasibility of fluid simulations in obtaining at least qualitative and, to some extent, quantitative features in the magnetized fluid. With continued improvements in the computational methods and computer resources, the usefulness and capability of the numerical approach should continue to improve.

Acknowledgements

This work was done under a grant from the Polish Ministry of Science for 2007–2010.

References

[1] Priest E R 1982 *Solar Magnetohydrodynamics*, Reidel Publishing Company, Dordrecht
[2] Godunov S K 1959 *Math. Sb.* **47** 271
[3] Stone J M and Norman M L 1992 *Astrophys. J. Suppl. Ser.* **80** 753
[4] Murawski K and Steinolfson R S 1996 *J. Geophys. Res.* **101** 2547
[5] Murawski K and Steinolfson R S 1996 *Planet. Space Sci.* **44** 243
[6] Woodward P R and Colella P 1984 *J. Comp. Phys.* **54** 115
[7] Roe P L and Balsara D S 1996 *SIAM J. Appl. Math.* **56** 57
[8] Barmin A A, Kulikovskiy A G and Pogorelov N V 1996 *J. Comp. Phys.* **126** 77
[9] Brackbill J U and Barnes D C 1980 *J. Comp. Phys.* **35** 426
[10] Brio M and Wu C C 1988 *J. Comp. Phys.* **75** 400
[11] Powell K G 1994 *ICASE Report*, No. 94-24, Langley, VA
[12] Brio M 1988 *J. Comp. Phys.* **75** 400
[13] Zachary A L and Colella P 1992 *J. Comp. Phys.* **99** 341
[14] Abeele D V 1995 *Development of a Godunov-type Solver for 2D Ideal MHD Problems*, van Karman Institute for Fluid Dynamics, Belgium
[15] Dellar P J 2001 *J. Comp. Phys.* **172** 392
[16] DeVore C R 1991 *J. Comp. Phys.* **92** 142
[17] Tanaka T 1993 *J. Geophys. Res.* **98** (17) 251
[18] Gombosi T I, De Zeeuw D L, Häberli R M and Powell K G 1994 *J. Geophys. Res.* **99** (21) 525
[19] Aslan N 1999 *J. Comp. Phys.* **153** 437

[20] Powell K G, Roe P L, Linde T J, Gombosi T I and De Zeeuw D L 1999 *J. Comp. Phys.* **154** 284
[21] Huynh H T 1995 *SIAM J. Numer. Anal.* **32** 1565
[22] Janhunen P 2000 *J. Comp. Phys.* **160** 649
[23] Balsara D S 1994 *Astrophys. J.* **420** 197
[24] Balsara D S 2001 *J. Comp. Phys.* **174** 614
[25] Tóth G 2000 *J. Comp. Phys.* **161** 605
[26] Tanaka T and Murawski K 1997 *J. Geophys. Res.* **102** (19) 805
[27] Tanaka T 1994 *J. Comp. Phys.* **111** 381
[28] Shyue K.-M. 2001 *J. Comp. Phys.* **171** 678
[29] Aschwanden M, Fletcher L, Schrijver C J and Alexander D 1999 *Astrophys. J.* **520** 880
[30] Aschwanden M 2003 *Proc. NATO Workshop*, Budapest, pp. 215–237
[31] Nakariakov V M 2003 *The Dynamic Sun*, (Dwivedi B, Ed.), CUP, pp. 314–334
[32] Williams D R, Mathioudakis M, Gallagher P T, Phillips K J H, McAteer R T J, Keenan F P, Rudawy P and Katsiyannis A C 2002 *MNRAS* **336** 747
[33] Nakariakov V M, Ofman L, Deluca E E, Roberts B and Davila J M 1999 *Science* **285** 862
[34] Nakariakov V M and Ofman L 2001 *Astron. Astrophys.* **372** L53
[35] Roberts B, Edwin P M and Benz A O 1984 *Astrophys J.* **279** 857
[36] Edwin P M and Roberts B 1983 *Solar Phys.* **88** 179
[37] Murawski K and Roberts B 1994 *Solar Phys.* **151** 305
[38] Murawski K, Aschwanden M and Smith J 1998 *Solar Phys.* **179** 313
[39] Zingale M, Dursi L J, ZuHone J, Calder A C, Fryxell B, Plewa T, Truran J W, Caceres A, Olson K and Ricker P M 2002 *Astrophys J. Suppl.* **143** 539
[40] Murawski K 2002 *Analytical and Numerical Methods for Wave Propagation in Fluids*, World Scientific, Singapore
[41] LeVeque R J 2002 *Finite-volume Methods for Hyperbolic Problems*, Cambridge
[42] Phillips J L and McComas D J 1991 *Space Sci. Rev.* **55** 1
[43] Zhang T L, Luhmann J G and Russell C T 1990 *J. Geophys. Res.* **95** (14) 961
[44] Khurana K K and Kivelson M G 1994 *J. Geophys. Res.* **99** 8505
[45] Luhmann J G, Russell C T, Scarf F L, Brace L H and Knudsen W C 1987 *J Geophys. Res.* **92** 8545
[46] Mahajan K K, Mayr H G, Brace L H and Cloutier P A 1989 *Geophys. Res. Lett.* **16** 759
[47] Zhang T L, Luhmann J G and Russell C T 1991 *J. Geophys. Res.* **96** (11) 145
[48] Brace L H, Hartle R E and Theis R F 1995 *Adv. Space Res.* **16** 99
[49] Brace L H and Kliore A J 1991 *Space Sci. Rev.* **55** 81
[50] Brace L H, Kasprzak W T, Taylor H A, Theis R F, Russell C T, Barnes A, Mihalov J D and Hunten D M 1987 *J. Geophys. Res.* **92** 15
[51] Brace L H, Theis R F, Mayr H G, Curtis S A and Luhmann J G 1982 *J. Geophys. Res.* **87** 199
[52] Marubashi K, Grebowsky J M, Taylor H A, Jr., Luhmann J G, Russell C T and Barnes A 1985 *J. Geophys. Res.* **90** 1385
[53] Tanaka T 1998 *Earth Planets Space* **50** 259
[54] Tanaka T 2000 *Adv. Space Res.* **26** 1577
[55] Tanaka T 1998 *J. Comm. Res. Lab.* **45** 119
[56] Cravens T E, Kliore A J, Kozyra J U and Nagy A F 1981 *J. Geophys. Res.* **86** (11) 323
[57] Phillips J L, Luhmann J G and Russell C T 1986 *J. Geophys. Res.* **91** 7931
[58] Tanaka T 1992 *Comp. Fluid Dyn. J.* **1** 14
[59] Phillips J L, Luhmann J G and Russell C T 1984 *J. Geophys. Res.* **89** (10) 676
[60] Brecht S H and Ferrante J R 1991 *J. Geophys. Res.* **96** (11) 209
[61] Keller C N and Cravens T E 1994 *J. Geophys. Res.* **99** 8505